

Bandgap Tuning in BaZrS₃ Perovskite Thin Films

Shyam Sharma, Zachary Ward, Kevin Bhimani, Kang Li, Aniruddha Lakhot, Rishabh Jain, Su-Fei Shi, Humberto Terrones, and Nikhil Koratkar*

Cite This: *ACS Appl. Electron. Mater.* 2021, 3, 3306–3312

Read Online

ACCESS |



Metrics & More

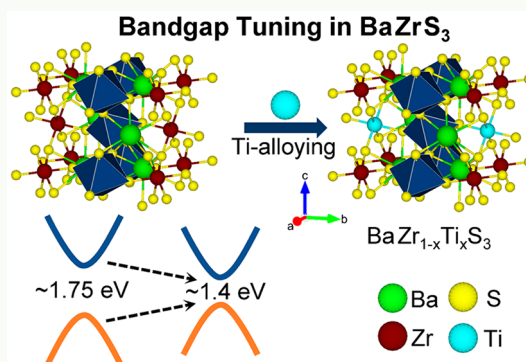


Article Recommendations



Supporting Information

ABSTRACT: Chalcogenide perovskites (such as BaZrS₃) are gaining increasing attention for solar cells due to their lead-free nature and superior environmental stability. However, a major limitation of BaZrS₃ is that its bandgap (~1.75 eV) is significantly larger than the ideal bandgap (~1.34 eV) required to achieve the maximum theoretical efficiency for a single-junction photovoltaic cell. In this study, we demonstrate the reduction in bandgap from 1.75 to 1.4 eV through in situ alloying of titanium (Ti) during chemical vapor deposition growth, forming BaZr_{1-x}Ti_xS₃ thin films. Theoretical study showed good agreement with experimental observations, demonstrating feasibility of bandgap tuning of BaZrS₃ films.



KEYWORDS: chalcogenide perovskites, BaZrS₃ thin films, Ti doping, band gap, Shockley–Queisser limit, solar cell

The United Nation's World Meteorological Organization report on the State of the Global Climate reported 2020 to be one of the three warmest on record despite the cooling effects of La Niña.¹ It highlighted the accelerating climate change indicators and their worsening impact on socio-economic development, migration, and food security for land/marine ecosystems. To address this challenge, some estimates indicate that global greenhouse gas emissions will need to be cut by 45% by 2030 from 2010 levels.² To achieve this target, the increase of the use of renewable energy is a must. Among available renewable technologies, the photovoltaic (PV) solar cell is a promising technology to convert solar energy into electricity.

Research in organic–inorganic hybrid perovskites for next generation optoelectronic devices has experienced very rapid growth.³ The progress to date has been remarkable: from a solar cell device efficiency of 3.8% in 2009⁴ to 29.5% in 2020,⁵ exceeding the maximum efficiency achieved by silicon solar cells. These perovskites offer excellent charge-carrier mobilities⁶ and lifetimes,⁷ resulting in high solar cell device efficiencies⁸ at low-cost using industry-scalable technologies.⁹ However, the achievement of their full potential will require us to overcome certain barriers related to their stability, environmental compatibility, and toxicity, but if these concerns are addressed, perovskite-based technology holds a transformational potential for large-scale solar cell deployment.

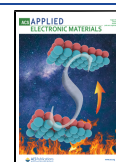
To address the stability and toxicity issue of organic–inorganic hybrid perovskites such as methylammonium lead halides (CH₃NH₃PbX₃), the use of chalcogenide perovskites ABX₃ (X = S, Se; A, B = metals with the combined valence of 6) was proposed through first-principle calculations for

optoelectronic applications.¹⁰ Subsequent experimental efforts were successful in synthesizing a number of chalcogenide perovskites.^{11–14} However, only CaZrS₃, CaHfS₃, BaZrS₃, and BaHfS₃ are expected to be suitable for solar cell applications from the carrier mobility point of view.^{15,16} Among these, BaZrS₃ perovskite is the ideal candidate for photovoltaic applications due to its lowest bandgap of ~1.7 eV out of the four.¹⁷ Wei et al. reported the synthesis of BaZrS₃ thin film with its distorted perovskite structure and strong light absorption properties.¹⁸ Our previous work has also demonstrated the superior environmental stability of BaZrS₃ thin films when compared to traditional organic–inorganic hybrid perovskites such as CH₃NH₃PbI₃.¹⁷ The lack of toxic lead (Pb), its intrinsic stability under photoexcitation, and moisture made this chalcogenide perovskite a viable candidate for optoelectronics.¹⁷ However, the ~1.7 eV bandgap of BaZrS₃ is significantly larger than the ideal bandgap required for photovoltaic applications. To achieve the maximum theoretical efficiency of ~33.7% (Shockley–Queisser limit) for a single junction photovoltaic cell, the bandgap must be ~1.34 eV.¹⁹ It has been shown theoretically that the bandgap of BaZrS₃ can be tuned through alloying with titanium (Ti), which lowers the conduction band minimum,¹⁵ and device simulations by

Received: June 29, 2021

Accepted: August 3, 2021

Published: August 6, 2021



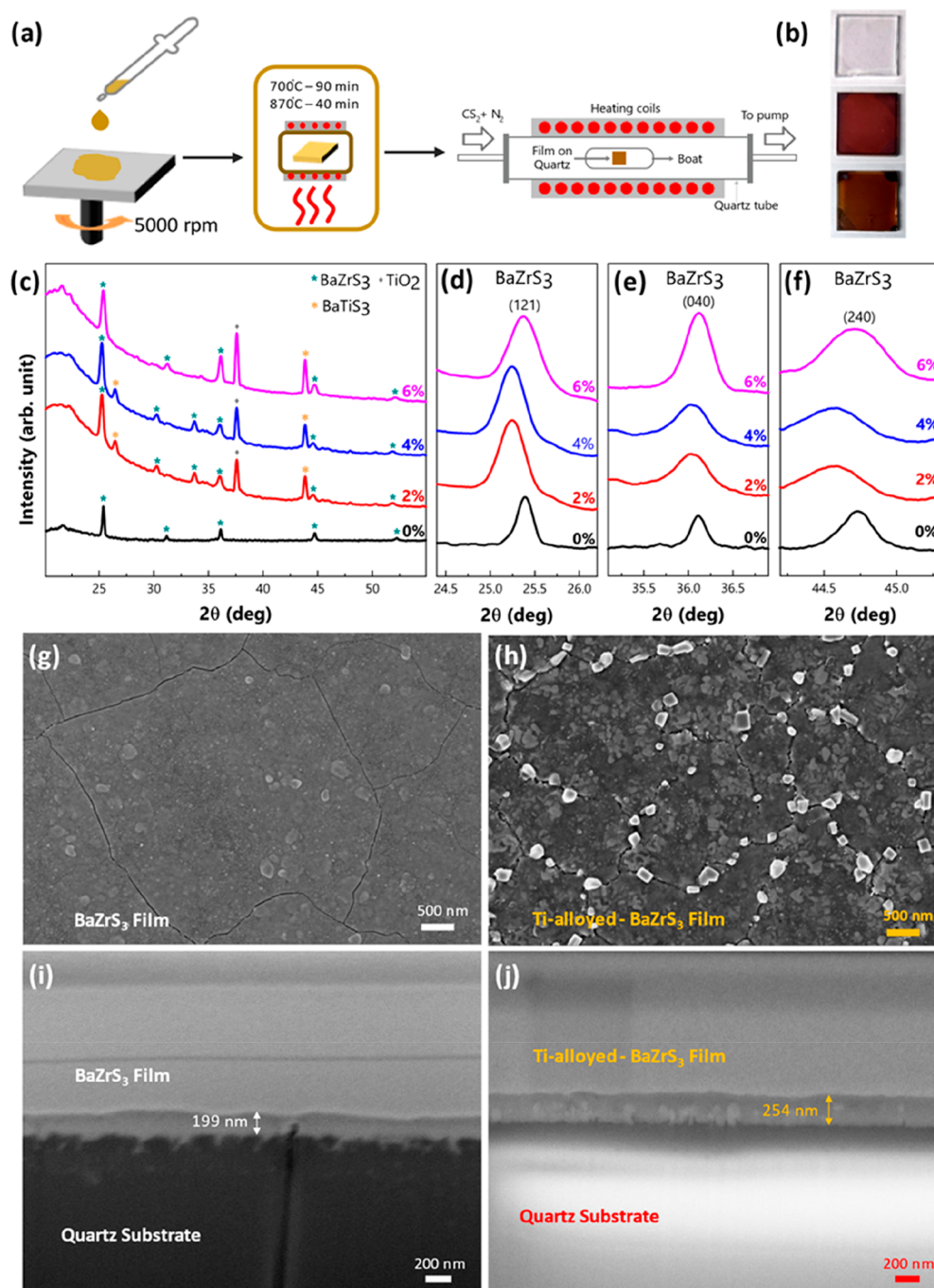


Figure 1. Synthesis and characterization of unalloyed and alloyed BaZrS_3 thin films. (a) Schematic illustrating the synthesis of BaZrS_3 -based perovskite films. (b) Optical images of BaZrO_3 (top), BaZrS_3 (middle), and Ti alloyed BaZrS_3 (bottom). (c–f) XRD pattern of unalloyed and alloyed BaZrS_3 films at different Ti concentrations of (c) 20–55, (d) 24.5–26.0, (e) 35–37, and (f) 44–45.5 (2θ degrees). (g, h) SEM images of (g) unalloyed BaZrS_3 film and (h) alloyed BaZrS_3 film. (i, j) FIB cross-sectional SEM images of (i) unalloyed BaZrS_3 film and (j) alloyed BaZrS_3 film. The Ti concentrations in (c–f) were taken from the molar ratio of the precursors used during film growth.

Nishigaki et al. have shown 38% efficiency in the $\text{Ba}(\text{Zr,Ti})\text{S}_3/\text{c-Si}$ tandem structure.²⁰ Some work has been published to show the reduction in BaZrS_3 bandgap with Ti alloying but through the powder synthesis approach,²¹ which is not viable for solar cell device fabrication (thin film synthesis is required to fabricate a photovoltaic cell). In this work, we have shown the synthesis of Ti-alloyed BaZrS_3 thin films with a reduced bandgap of ~ 1.4 eV, which is near the maximum efficiency range. We have also observed instability at higher alloying concentrations and have shown theoretical work on formation

energies to explain the reason. Such alloyed chalcogenide perovskite thin films with optimized band gap properties could offer improved photovoltaic solar cell performance.

A schematic illustration of the Ti-alloyed BaZrS_3 film synthesis process is shown in Figure 1a. The Ti-alloyed BaZrS_3 films were obtained by sulfurization of Ti-alloyed BaZrO_3 oxide films, which were synthesized by chemical solution deposition on a quartz substrate through spin coating followed by annealing in air. Additional details of the fabrication process are provided in the methods (Supporting Information).

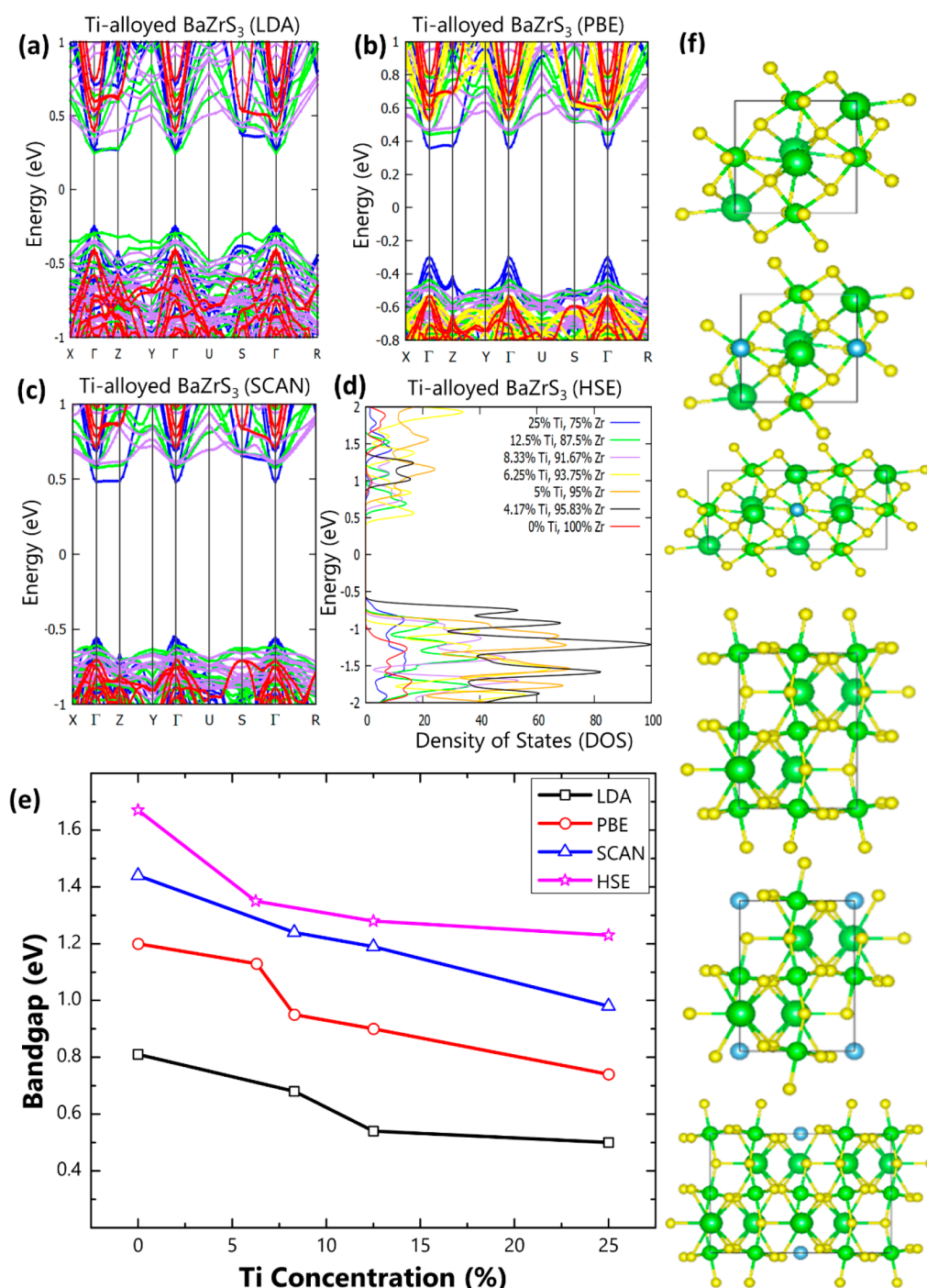


Figure 2. DFT assisted bandgap calculations. (a–c) Band structures for the BaZr_{1-x}Ti_xS₃ perovskite along the X-Γ-Z-Y-Γ-U-S-Γ-R path and bandgaps (eV) for different Ti-alloying concentrations: red (0% Ti, 100% Zr), yellow (6.3% Ti, 93.7% Zr), purple (8.3% Ti, 91.7% Zr), green (12.5% Ti, 87.5% Zr), and blue (25% Ti, 75% Zr) using the (a) LDA functional, (b) PBE functional, and (c) SCAN functional. (d) DOS using the HSE functional for different Ti-alloying concentrations including smaller concentrations shown in yellow (6.3% Ti, 93.7% Zr), orange (5% Ti, 95% Zr), and black (4.17% Ti, 95.83% Zr). (e) Bandgap variation with Ti concentrations calculated using different functionals. (f) Ti-alloyed BaZrS₃ perovskite supercells with one Ti atom introduced into the supercell. The supercell dimensions from top to bottom are 1 × 1 × 1 with no added Ti atoms, 1 × 1 × 1 with a single Ti atom introduced, and 2 × 1 × 1 with one Ti atom.

Optical images in Figure 1b confirm that, upon sulfurization, the oxide films changed from colorless to dark brown. In order to understand the crystal structure of the fabricated Ti-alloyed BaZrS₃ films, X-ray diffraction spectroscopy (XRD) was employed.

The XRD pattern of BaZrS₃ films with different Ti alloying (0 to 6%) is shown in Figure 1c. The majority of peaks match with the standard reference pattern of BaZrS₃ (ICDD 15-0327), confirming that the sample was polycrystalline and possesses an orthorhombic distorted perovskite structure with the *Pnma* space group. Secondary phases match ICDD 72-

Table 1. Lattice Parameters (*a*, *b*, *c*) and Unit Cell Angles (α , β , γ) for the BaZrS₃ Perovskite from Rietveld Analysis of Our Experimental XRD Data and Calculation Results for Different Functionals Used

experiment	PBE (w/DFT-D)	LDA	SCAN
<i>a</i> = 7.01 Å	<i>a</i> = 7.03 Å	<i>a</i> = 6.87 Å	<i>a</i> = 7.03 Å
<i>b</i> = 7.04 Å	<i>b</i> = 7.15 Å	<i>b</i> = 7.03 Å	<i>b</i> = 7.11 Å
<i>c</i> = 9.96 Å	<i>c</i> = 10.08 Å	<i>c</i> = 9.84 Å	<i>c</i> = 10.07 Å
$\alpha = \beta = \gamma = 90^\circ$	$\alpha = \beta = \gamma = 90^\circ$	$\alpha = \beta = \gamma = 90^\circ$	$\alpha = \beta = \gamma = 90^\circ$

1679 (BaTiS₃) and ICDD 01-0562 (TiO₂). The background signal in the pattern originates from the amorphous quartz substrate. The enlarged view of the (121), (040), and (240) peaks of Ti-alloyed BaZrS₃ can be seen in Figure 1d–f. A peak shift is observed at lower Ti-alloying concentrations, and an increase in secondary phases such as TiO₂ starts to take place at higher Ti-alloying concentrations. The increase in intensity of TiO₂ peaks and an increase in fwhm of BaZrS₃ peaks with an increase in Ti concentration indicate a reduced stability of BaZrS₃ at increasing Ti-alloying concentrations, which is consistent with our theoretical work discussed later. Note that the Ti concentrations listed in Figure 1c–f were taken from the molar ratio of the precursors used during film growth.

The morphology of as-synthesized films was studied using scanning electron microscopy with the assistance of a focused ion beam (details in the Supporting Information). SEM images of both BaZrS₃ and Ti-alloyed BaZrS₃ confirm the films to be continuous with some rough patches. This indicates that the sulfurization step did not rupture the oxide films shown in Figure 1g,h. The cross-section SEM images of BaZrS₃ and Ti-alloyed BaZrS₃ confirms that the films were highly dense with a thickness ranging from 200 to 260 nm (Figure 1i,j). This is the correct range of thickness for chalcogenide perovskite optoelectronic device applications⁸ including single junction PV cells.

In order to understand the impact of Ti alloying on the band gap of BaZrS₃ perovskites, density functional theory (DFT)^{22–27} calculations were done (simulation details are mentioned in the Supporting Information). Four different types of functionals, local density approximation (LDA), generalized gradient approximation (GGA-PBE) with the DFT-D correction, strongly correlated and appropriately normed (SCAN), and the Heyd–Scuseria–Ernzerhof (HSE), were used to calculate the band gap of BaZrS₃ perovskites with different Ti-alloying concentrations. We explored four different functionals to establish which one most closely replicates the experimental results. Figure 2f shows the Ti-alloyed BaZrS₃ perovskite supercells with dimensions of 1 × 1 × 1 with no added Ti atoms, 1 × 1 × 1 with a single Ti atom introduced, and 2 × 1 × 1 with one Ti atom. Table 1 shows the lattice parameters used for various functionals. The calculated parameters show a good match with the experimental values obtained from Rietveld refinement of our XRD data.

For all functionals, the bandgap vs the Ti concentration was determined, and the band structure along the X-Γ-Z-Y-Γ-U-S-Γ-R k-point path was calculated except for when HSE was used due to HSE being computationally expensive. In addition, the PBE relaxed coordinates were used for the HSE calculation, and the density of states (DOS) was calculated for HSE instead, as shown in Figure 2a–d. For all functionals studied, the bandgap decreases monotonically as a function of increasing Ti-dopant concentration, as shown in Figure 2e. For LDA, the bandgap is heavily underestimated, and the bandgap decreases less rapidly after an 8.3% Ti-alloying

concentration is introduced. In addition, flat electronic bands occur at the conduction and valence bands along the Γ-Z path with a Ti concentration of 25%, but lower Ti concentrations exhibit a direct bandgap at the Γ point (Figure 2a). PBE also underestimates the bandgap but not as significantly as LDA. There is a sharp decrease in the bandgap between a 6.3% and 8.3% Ti concentration when using PBE, and similar to LDA, a flat electronic band occurs along the Γ-Z path but only in the conduction band for a 25% Ti-alloying concentration (Figure 2b). SCAN gives a better bandgap estimate than both LDA and PBE, and the bandgap decreases linearly as a function of the Ti concentration and exhibits a flat electronic band in the conduction band along the Γ-Z path similar to PBE with a Ti concentration of 25% (Figure 2c). For HSE, the predicted pristine BaZrS₃ bandgap is the closest to the experimentally observed bandgap (~1.7 eV), making HSE the best functional to estimate the numerical value of the bandgap. The bandgap decreases asymptotically as a function of the Ti concentration, which is the closest to the experimental findings (see Figure 3e). When a Ti-alloying concentration of 6.3% to 8.3% is utilized, the bandgap is ~1.3 eV, which is nearest to the maximum efficiency described by the Shockley–Queisser limit.¹⁹ For LDA, PBE, and SCAN, the Ti alloying results in a roughly linear trend in the bandgap vs Ti concentration graphs, whereas HSE more closely replicates the asymptotic-like behavior found in the experimental observations. While HSE is the most precise, it is also the most computationally expensive of the functionals examined.

X-ray photoelectron spectroscopy was employed to investigate chemical bonds in Ti-alloyed BaZrS₃ and Ti-alloyed BaZrO₃ films (Figure 3a–c). A C–C bond, observed due to adsorbed carbon species on films at 284.6 eV binding energy, was used as a reference. High-resolution Zr 3d XPS spectra of Ti-alloyed BaZrO₃ shows the appearance of three peaks at ~177.5, ~181, and ~184 eV, which can be attributed to Ba 4p, 3d_{5/2}, and 3d_{3/2} spin–orbital doublets of the Zr–O bond, respectively (Figure 3a). Similarly, in the case of Ti-alloyed BaZrS₃, three peaks at ~179, 182.5, and ~185 eV were observed, which can be attributed to Ba 4p, Zr–O/Zr–S 3d_{5/2}, and Zr–O/Zr–S 3d_{3/2}, respectively. The observation of the slight right shift in the XPS peaks can be due to the loss of electrons by Zr during sulfurization. An increase in relative intensity of the Ba 4p XPS peak can be attributed to a decrease in Zr concentration due to an increase in the amount of Ti alloying. According to the NIST XPS database, Zr–O and Zr–S bonds appear almost at the same binding energy, making it difficult for us to distinguish. High-resolution Ti 2p XPS spectra of Ti-alloyed BaZrO₃ shows the appearance of two peaks at ~458 and ~463.5 eV and can be attributed to the 2p_{3/2} and 2p_{1/2} spin–orbital doublet of Ti–O, respectively (Figure 3b). However, in the case of Ti-alloyed BaZrS₃, four peaks appeared at ~455, 458.5, ~463, and ~465 eV and can be attributed to Ti–S 2p_{3/2}, Ti–O 2p_{3/2}, Ti–S 2p_{1/2}, and Ti–O 2p_{1/2}, respectively. This confirms the successful alloying of Ti

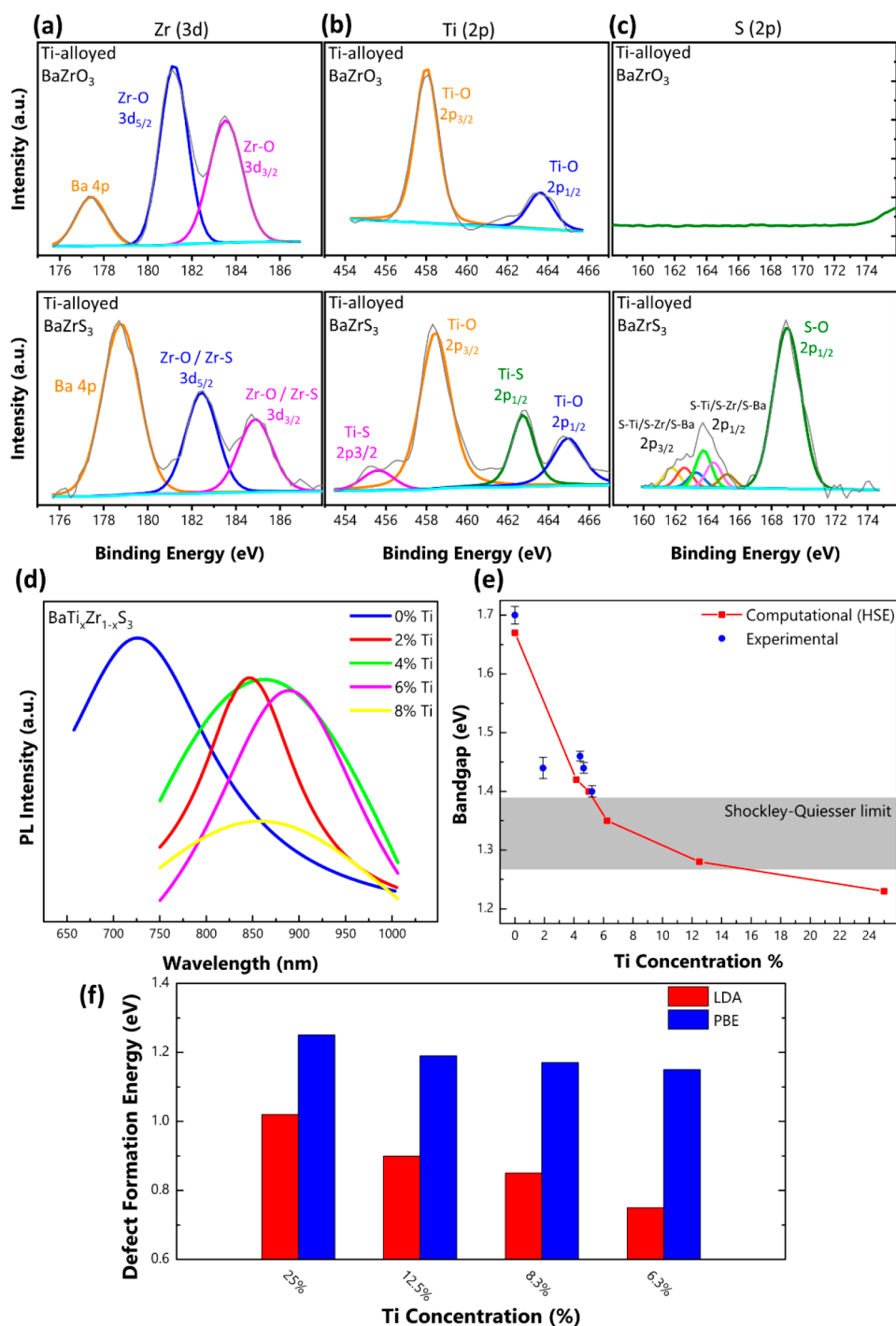


Figure 3. (a–c) High resolution X-ray photoelectron spectroscopy of BaTi_{0.04}Zr_{0.96}O₃ and BaTi_{0.06}Zr_{0.94}S₃ showing Zr (3d), Ti (2p), and S (2p) spectra. (d) Photoluminescence of BaTi_xZr_{1-x}S₃ films at different Ti-alloying concentrations. (e) Experimental and calculated (using HSE functional) bandgap variation with Ti concentration. The optimal bandgap range (from Shockley–Queisser theory) for PV materials is shown in the graph as the gray colored band. (f) Formation energies for the Ti-alloyed BaZrS₃ perovskite for different Ti concentrations calculated from the LDA and PBE functionals. Note that Ti concentration values in (d) are taken on the basis of the molar ratio of the precursors used during growth, while in (e), the Ti concentrations were obtained from XPS spectroscopy.

in BaZrS₃. In the case of high-resolution O 1s XPS spectra, Ti-alloyed BaZrO₃ shows the appearance of two peaks at ~529 and ~531 eV, which can be attributed to Zr–O/Ba–O and Ti–O peaks. However, in the case of Ti-alloyed BaZrS₃, only one peak appears at ~532.5 eV due to Ti–O. This confirms the successful sulfurization of the film. Lastly, in the case of Ti-alloyed BaZrO₃, no sulfur presence was observed, whereas Ti-

alloyed BaZrS₃ shows a considerable amount of sulfur, further indicating successful sulfurization. High-resolution S 2p XPS spectra in Ti-alloyed BaZrS₃ shows a very broad peak in ~160–166 eV and can be deconvoluted into 2p_{3/2} and 2p_{1/2} spin–orbital doublets of Zr–S, Ti–S, and Ba–S. The peak around ~169 eV can be due to SO_x^{y-}. Overall, XPS analysis confirms the successful synthesis of Ti-alloyed BaZrS₃ thin

films. The atomic percentage of Ti was also calculated from the XPS survey by averaging multiple points on the film and is used in Figure 3e to show the experimental vs HSE bandgap variation with Ti concentration.

Photoluminescence (PL) spectroscopy was employed to experimentally verify the change in band gap in BaZrS₃ due to Ti alloying. As shown in Figure 3d, pure BaZrS₃ films (with no Ti alloying) show a broad peak centered at ~725 nm wavelength, which corresponds to a band gap of ~1.75 eV. This is consistent with previously calculated and reported values.^{10,17} With the increase in Ti-alloying concentration (0 to 6%), three major differences in PL spectroscopy were observed: (1) a red-shift in the wavelength of the maximum PL intensity indicated a reduction in the bandgap of BaZrS₃ from 1.7 to 1.4 eV with Ti alloying. Such variation in the band gap is consistent with our bandgap calculations using HSE functional DFT (Figure 3e). The drop in the band gap to 1.4 eV is close to the maximum efficiency range described by the Shockley–Queisser theory for single-junction solar cells. (2) Significant quenching of the PL intensity indicated the formation of recombination centers due to an increase in defects resulting from Ti alloying and secondary phase formation. (3) Broadness in the PL peaks further indicated heterogeneity and defect formation (especially at higher alloying concentration). Note that the PL peak widths did not show a clear trend with respect to Ti-alloying concentration. We expect this is because, as the film quality becomes more heterogeneous (i.e., less uniform), there will be changes in peak width depending on the location from which the PL data is extracted.

No further reductions in the bandgap for Ti-alloying concentrations above 6% were observed in the experiments and can be due to phase separation at higher Ti-alloying levels. For example, the PL spectra of the 8% Ti-alloying film (Figure 3d) shows both quenching of the PL intensity and a slightly higher bandgap than the 6% sample. Therefore, there is no further benefit to be gained by going above an ~6% Ti concentration. The stability of Ti-alloyed BaZrS₃ perovskites was evaluated by calculating the formation energies (E_{form}) using the relation:

$$E_{\text{form}} = E_{\text{Ti-BaZrS}_3} - E_{\text{BaZrS}_3} + E_{\text{Zr}} - E_{\text{Ti}}$$

where E_{BaZrS_3} is the pristine BaZrS₃ energy, $E_{\text{Ti-BaZrS}_3}$ is the Ti-alloyed BaZrS₃ energy, and E_{Zr} and E_{Ti} are the elemental energies for Zr and Ti, respectively, obtained from the LDA and PBE functionals. Figure 3f shows that, with an increase in Ti concentration, the perovskite becomes less stable (i.e., more prone to defects), which is in agreement with our XRD and PL results. This explains why increasing the Ti-alloying concentration beyond ~6% was not possible in the experiments.

To conclude, we have successfully synthesized Ti-alloyed BaZrS₃ thin films through a facile chemical vapor deposition technique based on the sulfurization of oxide films. At lower Ti-alloying concentrations (up to 6%), the films show a reduction in bandgap from 1.75 to 1.4 eV, which is near the maximum efficiency range described by the Shockley–Queisser limit.¹⁹ In contrast to this, higher Ti-alloying concentrations (>6%) yield destabilization of the chalcogenide perovskite phase, which is consistent with our theoretical work.

Optimal bandgap combined with the nontoxicity and high environmental stability of these films can make Ti-alloyed BaZrS₃ thin films a promising candidate for optoelectronic

devices. Besides Ti, other possible alloying elements (Ca, Hf, La, etc.) should be considered as part of the future work and compared to Ti-alloyed BaZrS₃ films. A concern, though, is the high-temperature synthesis, which is not compatible with device fabrication and also leads to rough film surface morphology. Therefore, future work should also focus on reducing the synthesis temperature of these films.

■ ASSOCIATED CONTENT

Supporting Information

The Supporting Information is available free of charge at <https://pubs.acs.org/doi/10.1021/acsaelm.1c00575>.

Methods including the synthesis of Ti-alloyed BaZrO₃ thin film, the synthesis of Ti-alloyed BaZrS₃ thin film, materials characterization, and computational details (PDF)

■ AUTHOR INFORMATION

Corresponding Author

Nikhil Koratkar – Department of Materials Science and Engineering and Department of Mechanical, Aerospace, and Nuclear Engineering, Rensselaer Polytechnic Institute, Troy, New York 12180, United States; orcid.org/0000-0002-4080-3786; Email: koratn@rpi.edu

Authors

Shyam Sharma – Department of Materials Science and Engineering, Rensselaer Polytechnic Institute, Troy, New York 12180, United States

Zachary Ward – Department of Physics, Applied Physics, and Astronomy, Rensselaer Polytechnic Institute, Troy, New York 12180, United States

Kevin Bhimani – Department of Mechanical, Aerospace, and Nuclear Engineering, Rensselaer Polytechnic Institute, Troy, New York 12180, United States

Kang Li – Department of Chemical and Biological Engineering, Rensselaer Polytechnic Institute, Troy, New York 12180, United States

Aniruddha Lakhnot – Department of Mechanical, Aerospace, and Nuclear Engineering, Rensselaer Polytechnic Institute, Troy, New York 12180, United States

Rishabh Jain – Department of Mechanical, Aerospace, and Nuclear Engineering, Rensselaer Polytechnic Institute, Troy, New York 12180, United States

Su-Fei Shi – Department of Chemical and Biological Engineering, Rensselaer Polytechnic Institute, Troy, New York 12180, United States; orcid.org/0000-0001-5158-805X

Humberto Terrones – Department of Physics, Applied Physics, and Astronomy, Rensselaer Polytechnic Institute, Troy, New York 12180, United States; orcid.org/0000-0003-0515-0721

Complete contact information is available at: <https://pubs.acs.org/doi/10.1021/acsaelm.1c00575>

Notes

The authors declare no competing financial interest.

■ ACKNOWLEDGMENTS

N.K. and H.T. acknowledge funding support from the USA National Science Foundation (Award 2013640). S.-F.S. acknowledges support from the NSF through Career Award DMR-1945420 and Grant DMR-2104902. H.T. and Z.W. are

grateful to the “Extreme Science and Engineering Discovery Environment” (XSEDE), which is supported by National Science Foundation grant number ACI-1548562 through proposal TG-DMR170008.

REFERENCES

- (1) World Meteorological Organization (WMO). *The State of the Global Climate 2020*; WMO, 2021.
- (2) Ho, M. S.; Nielsen, C. P., Eds.; Summary for Policy. In *Clearing the Air*; MIT Press, 2007; DOI: 10.7551/mitpress/1866.003.0006.
- (3) Deschler, F.; Neher, D.; Schmidt-Mende, L. Perovskite Semiconductors for next Generation Optoelectronic Applications. *APL Materials* **2019**, *7*, 80401.
- (4) Kojima, A.; Teshima, K.; Shirai, Y.; Miyasaka, T. Organometal Halide Perovskites as Visible-Light Sensitizers for Photovoltaic Cells. *J. Am. Chem. Soc.* **2009**, *131* (17), 6050–6051.
- (5) NREL. *Best Research-Cell Efficiency Chart*; <https://www.nrel.gov/pv/cell-efficiency.html>.
- (6) Herz, L. M. Charge-Carrier Mobilities in Metal Halide Perovskites: Fundamental Mechanisms and Limits. *ACS Energy Letters* **2017**, *2*, 1539–1548.
- (7) DeQuilettes, D. W.; Vorpahl, S. M.; Stranks, S. D.; Nagaoka, H.; Eperon, G. E.; Ziffer, M. E.; Snaith, H. J.; Ginger, D. S. Impact of Microstructure on Local Carrier Lifetime in Perovskite Solar Cells. *Science (Washington, DC, U. S.)* **2015**, *348* (6235), 683–686.
- (8) Sha, W. E. I.; Ren, X.; Chen, L.; Choy, W. C. H. The Efficiency Limit of CH₃NH₃PbI₃ Perovskite Solar Cells. *Appl. Phys. Lett.* **2015**, *106* (22), 221104.
- (9) Yin, W. J.; Shi, T.; Yan, Y. Unique Properties of Halide Perovskites as Possible Origins of the Superior Solar Cell Performance. *Adv. Mater.* **2014**, *26* (27), 4653–4658.
- (10) Sun, Y. Y.; Agiorgousis, M. L.; Zhang, P.; Zhang, S. Chalcogenide Perovskites for Photovoltaics. *Nano Lett.* **2015**, *15* (1), 581–585.
- (11) Hanzawa, K.; Iimura, S.; Hiramatsu, H.; Hosono, H. Material Design of Green-Light-Emitting Semiconductors: Perovskite-Type Sulfide SrHfS₃. *J. Am. Chem. Soc.* **2019**, *141* (13), 5343–5349.
- (12) Niu, S.; Huyan, H.; Liu, Y.; Yeung, M.; Ye, K.; Blankemeier, L.; Orvis, T.; Sarkar, D.; Singh, D. J.; Kapadia, R.; Ravichandran, J. Bandgap Control via Structural and Chemical Tuning of Transition Metal Perovskite Chalcogenides. *Adv. Mater.* **2017**, *29* (9), 1604733.
- (13) Perera, S.; Hui, H.; Zhao, C.; Xue, H.; Sun, F.; Deng, C.; Gross, N.; Milleville, C.; Xu, X.; Watson, D. F.; Weinstein, B.; Sun, Y. Y.; Zhang, S.; Zeng, H. Chalcogenide Perovskites - an Emerging Class of Ionic Semiconductors. *Nano Energy* **2016**, *22*, 129–135.
- (14) Handa, T.; Wakamiya, A.; Kanemitsu, Y. Photophysics of Lead-Free Tin Halide Perovskite Films and Solar Cells. *APL Materials* **2019**, *7*, 080903.
- (15) Meng, W.; Saparov, B.; Hong, F.; Wang, J.; Mitzi, D. B.; Yan, Y. Alloying and Defect Control within Chalcogenide Perovskites for Optimized Photovoltaic Application. *Chem. Mater.* **2016**, *28* (3), 821–829.
- (16) Lelieveld, R.; Ijdo, D. J. W. Sulfides with the GdFeO₃ Structure. *Acta Crystallogr., Sect. B: Struct. Crystallogr. Cryst. Chem.* **1980**, *36* (10), 2223–2226.
- (17) Gupta, T.; Ghoshal, D.; Yoshimura, A.; Basu, S.; Chow, P. K.; Lakshmi, A. S.; Pandey, J.; Warrender, J. M.; Efsthadiadis, H.; Soni, A.; Osei-Agyemang, E.; Balasubramanian, G.; Zhang, S.; Shi, S. F.; Lu, T. M.; Meunier, V.; Koratkar, N. An Environmentally Stable and Lead-Free Chalcogenide Perovskite. *Adv. Funct. Mater.* **2020**, *30* (23), 2001387.
- (18) Wei, X.; Hui, H.; Zhao, C.; Deng, C.; Han, M.; Yu, Z.; Sheng, A.; Roy, P.; Chen, A.; Lin, J.; Watson, D. F.; Sun, Y. Y.; Thomay, T.; Yang, S.; Jia, Q.; Zhang, S.; Zeng, H. Realization of BaZrS₃ Chalcogenide Perovskite Thin Films for Optoelectronics. *Nano Energy* **2020**, *68*, 104317.
- (19) Shockley, W.; Queisser, H. J. Detailed Balance Limit of Efficiency of P-n Junction Solar Cells. *J. Appl. Phys.* **1961**, *32* (3), 510–519.
- (20) Nishigaki, Y.; Nagai, T.; Nishiwaki, M.; Aizawa, T.; Kozawa, M.; Hanzawa, K.; Kato, Y.; Sai, H.; Hiramatsu, H.; Hosono, H.; Fujiwara, H. Extraordinary Strong Band-Edge Absorption in Distorted Chalcogenide Perovskites. *Sol. RRL* **2020**, *4* (5), 1900555.
- (21) Wei, X.; Hui, H.; Perera, S.; Sheng, A.; Watson, D. F.; Sun, Y. Y.; Jia, Q.; Zhang, S.; Zeng, H. Ti-Alloying of BaZrS₃ Chalcogenide Perovskite for Photovoltaics. *ACS Omega* **2020**, *5* (30), 18579–18583.
- (22) Perdew, J. P.; Zunger, A. Self-Interaction Correction to Density-Functional Approximations for Many-Electron Systems. *Phys. Rev. B: Condens. Matter Mater. Phys.* **1981**, *23* (10), 5048–5079.
- (23) Perdew, J. P. Density-Functional Approximation for the Correlation Energy of the Inhomogeneous Electron Gas. *Phys. Rev. B: Condens. Matter Mater. Phys.* **1986**, *33* (12), 8822–8824.
- (24) Grimme, S. Semiempirical GGA-Type Density Functional Constructed with a Long-Range Dispersion Correction. *J. Comput. Chem.* **2006**, *27* (15), 1787–1799.
- (25) Sun, J.; Remsing, R. C.; Zhang, Y.; Sun, Z.; Ruzsinszky, A.; Peng, H.; Yang, Z.; Paul, A.; Waghmare, U.; Wu, X.; Klein, M. L.; Perdew, J. P. SCAN: An Efficient Density Functional Yielding Accurate Structures and Energies of Diversely-Bonded Materials. *arXiv*, **2015**, 1511.01089.
- (26) Heyd, J.; Scuseria, G. E. Efficient Hybrid Density Functional Calculations in Solids: Assessment of the Heyd-Scuseria-Ernzerhof Screened Coulomb Hybrid Functional. *J. Chem. Phys.* **2004**, *121* (3), 1187–1192.
- (27) Ghathian, H. M.; Alahmed, Z. A.; Qaid, S. M. H.; Hezam, M.; Aldwayyan, A. S. Density Functional Study of Cubic, Tetragonal, and Orthorhombic CsPbBr₃ Perovskite. *ACS Omega* **2020**, *5* (13), 7468–7480.